RSC Advances

PAPER

View Article Online
View Journal | View Issue

Cite this: *RSC Adv.*, 2022, **12**, 18197

Theoretical study on the mechanism, chemo- and enantioselectivity of the Ag- *vs.* Rh-catalyzed intramolecular carbene transfer reaction of diazoacetamides†

Qingmin Song,[a] Jiayi Wu,[a] Nikolaos V. Tzoukras,[b] Yong Wu *[a] and Steven P. Nolan *[b]

Received 26th February 2022
Accepted 13th June 2022

DOI: 10.1039/d2ra01298g

rsc.li/rsc-advances

To explore the mechanism of silver and rhodium catalysis and reveal the origin of the chemo- and enantioselectivity of the reaction, density functional theory calculations were performed on the first silver-catalyzed highly enantioselective carbene transfer reaction. The calculation results reveal that when silver is used as a catalyst, due to the participation of the phosphate anion in the transition state, the enhanced nucleophilicity of the α-diazoacetamide unit promotes smooth dearomatization before generation of the silver carbene. Because the generated rhodium carbene has stronger electrophilicity, typical carbene reactions (C–H insertion and the Büchner reaction) are favored. In addition, in the process of silver catalyzed dearomatization, the formation of an R-type transition state is determined by the small torsion energy and strong interaction energy.

Introduction

Metal carbenes are a class of highly reactive intermediates, and their catalytic transformations have developed into a very important field in organic synthetic chemistry.[1] Compared with widely used catalysts based on metals such as rhodium, copper and gold, silver-based catalysts exhibit unique reactivity and selectivity.[2–5] At present, some research groups have successfully realized metal carbene mediated selective addition to arenes.[6] However, the field of silver-catalyzed asymmetric carbene transfer reactions has developed very slowly[7–11] because of the linear and triangular coordination modes,[12] the competitive Lewis acid-catalyzed pathway and the free carbene pathway.[13] Since 1996, Burgess,[14] Jørgensen[13] and others[10,11,15,16] have investigated the asymmetric carbene transfer reaction catalyzed by silver salts, but have not achieved satisfactory results. In 2017, Nemoto's research group successfully realized the first silver-catalyzed, highly enantioselective carbene transfer reaction through the intramolecular reaction model.[9] They deployed (*S*)-TRIPAg as a catalyst to achieve the asymmetric dearomatization of phenols with α-diazoamides under mild conditions (Fig. 1). The chiral catalyst can effectively induce the configuration of the product, by circumventing the long distance between the chiral center and the reaction center, which leads to weakening of the induction effect. In this reaction, silver catalysis exhibits high chemoselectivity, effectively preventing the Büchner reaction and the C–H insertion reaction.

Since then, asymmetric carbene transfer reactions based on silver catalysis have been successively developed. In these reaction systems, the use of a silver catalyst was essential for achieving high chemo- and enantioselectivity. However, the reasons for the efficient catalysis of silver salts and the origin of the metal-determined chemo- and enantioselectivity remain unclear. Therefore, this work adopts the work of Nemoto's group as a model, and deeply explores the mechanism of the intramolecular carbene transfer reaction catalyzed by (*S*)-TRIPAg and $Rh_2(OAc)_4$ through density functional theory (DFT) calculations. The optimal path of different, transition metal-catalyzed reactions and the key factors affecting the chemo- and enantioselectivity of the reaction are revealed. A deeper understanding of the mechanism should help provide some insights for the further development of metal-catalyzed carbene transfer reactions and silver chemistry.

Computational details

All DFT calculations were performed using Gaussian16 suite of program.[17] All structure geometries were optimized without any symmetry constraints in the gas phase by using B3LYP[18] functional with D3BJ dispersion corrections,[19] and a mixed basis set of SDD[20] for the transition metals and 6-31G(d,p) for other atoms. Frequency calculations were performed at the same

[a]*Department of Chemistry Northeast Normal University, Changchun 130024, China. E-mail: wuy651@nenu.edu.cn*

[b]*Department of Chemistry and Center for Sustainable Chemistry, Ghent University, Krijgslaan 281, S3, Ghent 9000, Belgium. E-mail: Steven.Nolan@UGent.be*

† Electronic supplementary information (ESI) available. See https://doi.org/10.1039/d2ra01298g

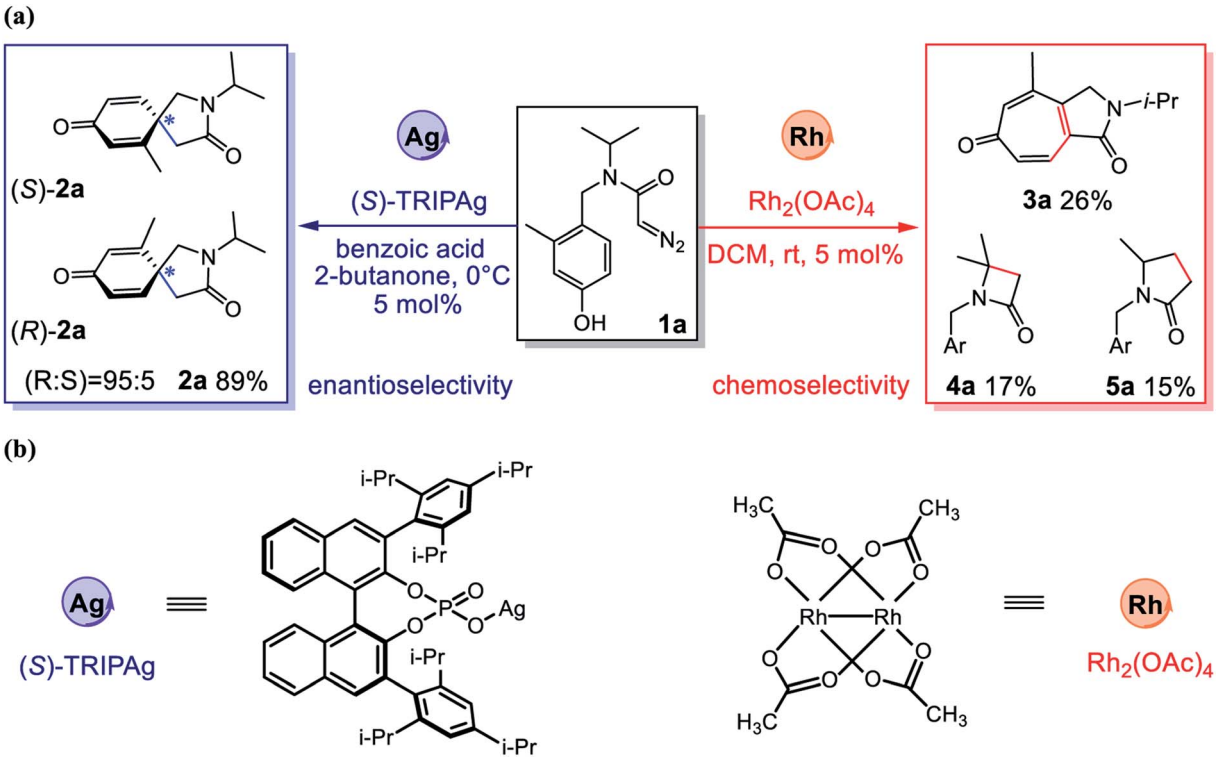

Fig. 1 (a) Asymmetric intramolecular dearomatization, 1°/3° C–H insertion and Büchner reaction of α-diazoamide **1a** catalyzed by Ag/Rh; (b) the structures for Ag and Rh catalysts.

theoretical level for all optimized geometries to confirm them as minima (zero imaginary frequencies) or transition-state structures (a single imaginary frequency). Intrinsic reaction coordinate (IRC)[21] were traced from the various transition structures to obtain the connected intermediates. Single-point energies were calculated at the ωB97XD/6-311+G(d,p) level of theory with the SMD[22] solvation model. Dichloromethane was chosen as solvent for rhodium catalytic system, while butanone was used as solvent for silver catalytic system. Non-covalent interaction (NCI) analysis and energy decomposition analysis (EDA) were calculated by the Multiwfn program.[23] Three-dimensional diagrams of the computed species were generated using CYLview visualization software.[24]

Results and discussion

Based on the experimental results, DFT calculations on the asymmetric intramolecular dearomatization of α-diazoamide **1a** catalyzed by (*S*)-TRIPAg, the Büchner reaction and the 1°/3° C–H insertion reaction catalyzed by $Rh_2(OAc)_4$ were carried out to further explore the origins of chemical selectivity and enantioselectivity. Firstly, we propose three possible reaction mechanisms catalyzed by metal salts, as shown in Fig. 2.

Starting from metal carbene intermediates, there are three reaction pathways: (1) chiral spiro cyclization occurs through intramolecular electrophilic addition, followed by intramolecular protodemetalation to obtain azaspiro[4.5]decane

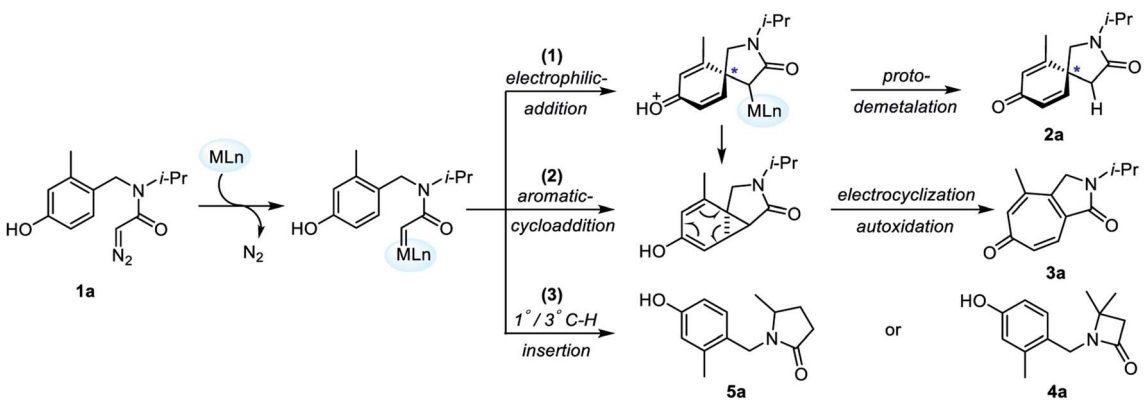

Fig. 2 Mechanistic pathways of transition metal-catalyzed intramolecular carbene transfer reaction of α-diazoamide **1a**.

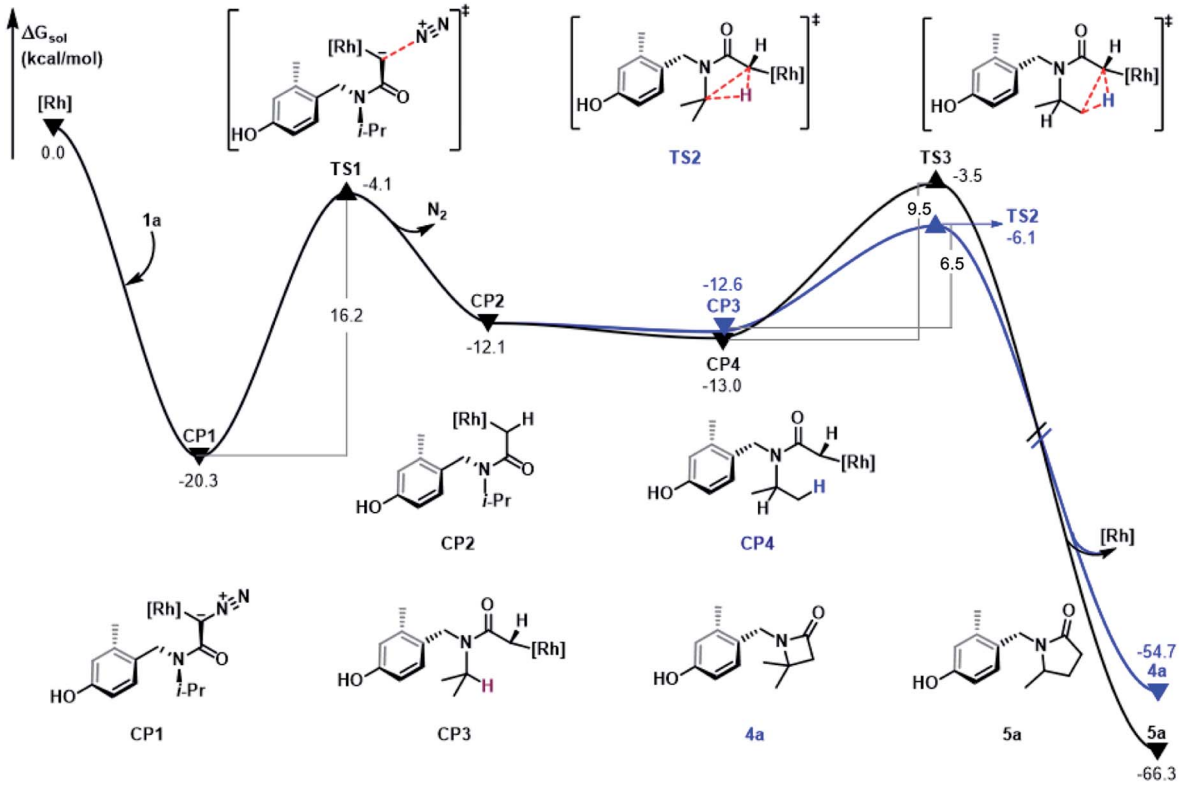

Fig. 3 Gibbs free energy profile (in kcal mol^{-1}) for the pathways of 1°/3° C–H insertion reaction of α-diazoamide **1a** catalyzed by $Rh_2(OAc)_4$.

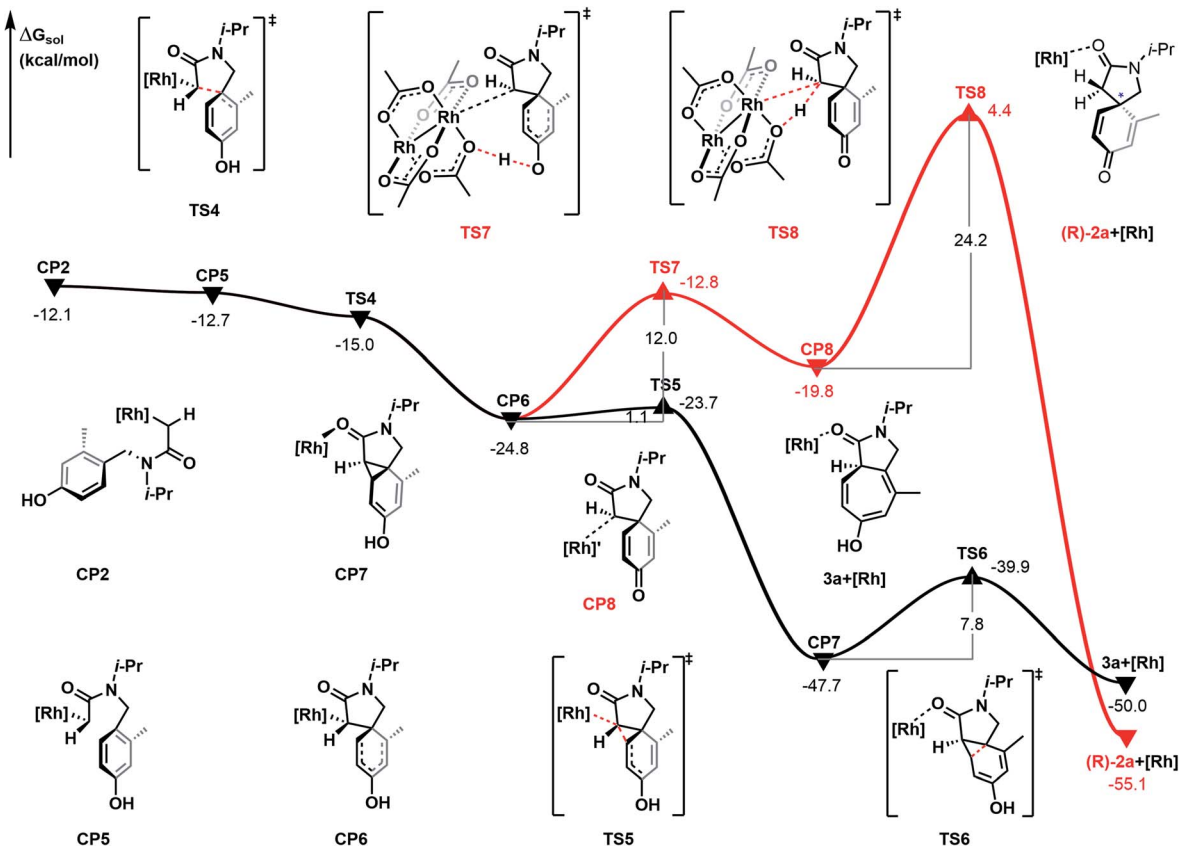

Fig. 4 Gibbs free energy profile (in kcal mol^{-1}) for the Büchner reaction mechanism catalyzed by $Rh_2(OAc)_4$.

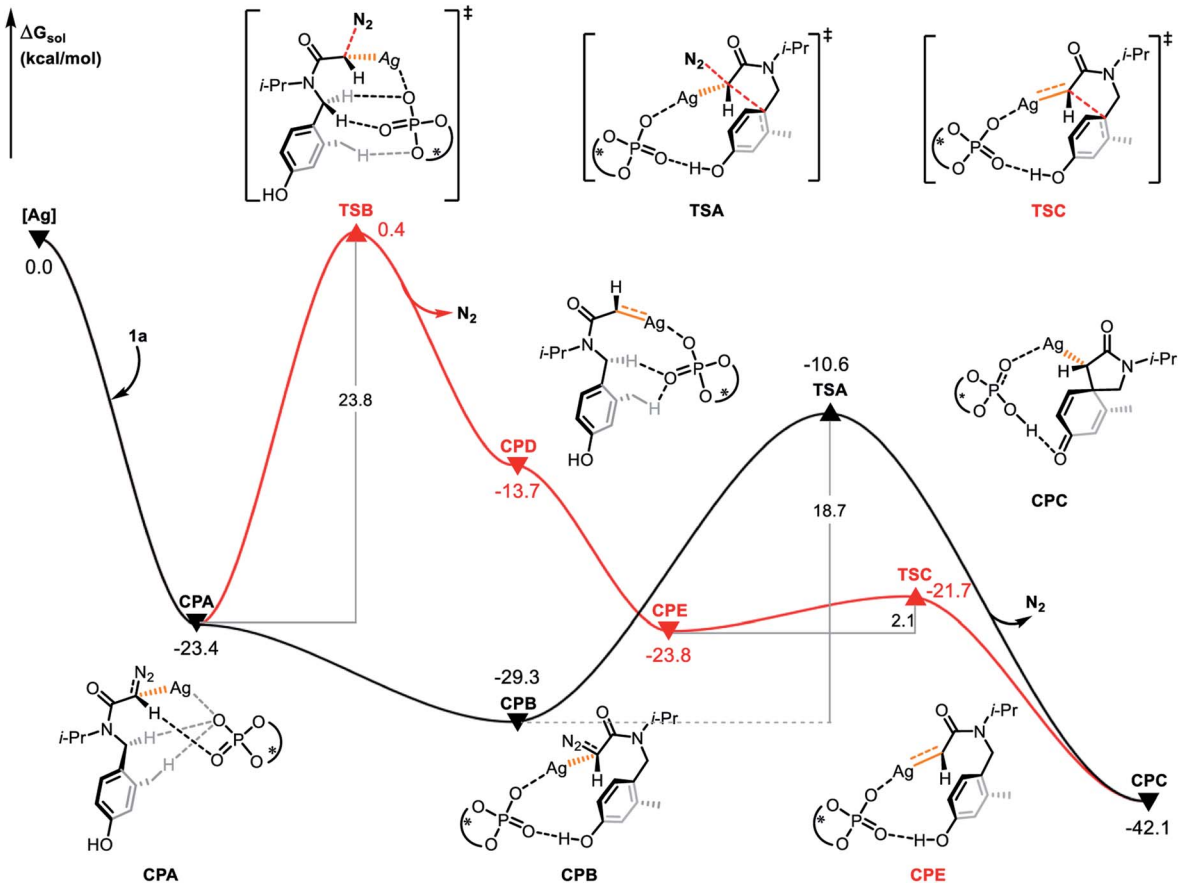

Fig. 5 Gibbs free energy profile (in kcal mol^{-1}) for the electrophilic addition of *R* configuration catalyzed by chiral silver phosphate.

derivative **2a**. (2) Through aromatic cycloaddition to form ternary ring intermediates; subsequently, cycloheptatrienone **3a** is obtained by ring enlargement and autoxidation. (3) The metal carbene complex leads to γ-lactam **5a** or β-lactam **4a** by an intramolecular 1°/3° C–H insertion reaction. Considering these three reaction pathways, DFT calculations were performed to reveal the mechanism of Ag and Rh catalyzed intramolecular carbene transfer reactions.

Mechanism of the 1°/3° C–H insertion reaction catalyzed by $Rh_2(OAc)_4$

In Fig. 3, the free energy profile of C–H bond insertion is shown based on the mechanism discussed above and the energy profile is discussed using $Rh_2(OAc)_4$ as the starting point. The substrate, α-diazoacetamide **1a**, contains a formal N≡N triple bond and a negatively charged α-carbon. The α-carbon site is coordinated with the metal center of the rhodium salt to form the stable complex **CP1** and this step is exothermic by an energy difference of 20.3 kcal mol^{-1}. Subsequent denitrogenation of **CP1** occurs *via* transition state **TS1** by cleavage of the C–N bond with an energy barrier of 16.2 kcal mol^{-1}, to give rhodium-carbene complex **CP2**, a process which is endergonic by 8.2 kcal mol^{-1}. **CP2** undergoes isomerization following the C–N bond rotation and generates the intermediates **CP3** and **CP4**, steps which are exothermic by 0.5 kcal mol^{-1} and 0.9 kcal mol^{-1}, respectively. The generation of intermediates **CP3** and **CP4** facilitate the C–H insertion and then the C–C bond generation. Comparing the two reaction paths, shows that their energy barrier difference is only 3.0 kcal mol^{-1}, which is consistent with the experimental results of obtaining **4a** and **5a** products with 17% and 15% yields, respectively.

The Büchner reaction mechanism

As shown in Fig. 4, the Büchner reaction mechanism has been explored, taking the rhodium-carbene complex **CP2** as the starting point of the energy profile. Activation of 4 °C contains two steps, cyclopropanation and ring-expansion reactions. Firstly, **CP2** undergoes isomerization following the C–N bond rotation and generates the intermediate **CP5**, a step which is exothermic by 0.6 kcal mol^{-1}. The intermediate **CP5** leads to the electrophilic addition reaction. Intramolecular C–C bond formation between the C-atom of Rh-carbene and the C-atom of the phenyl to generate spirocyclic intermediate **CP6**, with a free energy release of 12.1 kcal mol^{-1}. Subsequently, the 5 membered ring of **CP6** undergoes aromatic-addition *via* the transition state **TS5** to form the cyclopropane **CP7**, with a free energy release of 22.9 kcal mol^{-1} and the energy barrier of this step is 1.1 kcal mol^{-1}. In the next step, the $C_{sp}{}^2$–$C_{sp}{}^3$ bond of the fused ring of **CP6** is cleaved and generates the ring-expansion product **3a**, with a relative free energy of −50.0 kcal mol^{-1}. Of

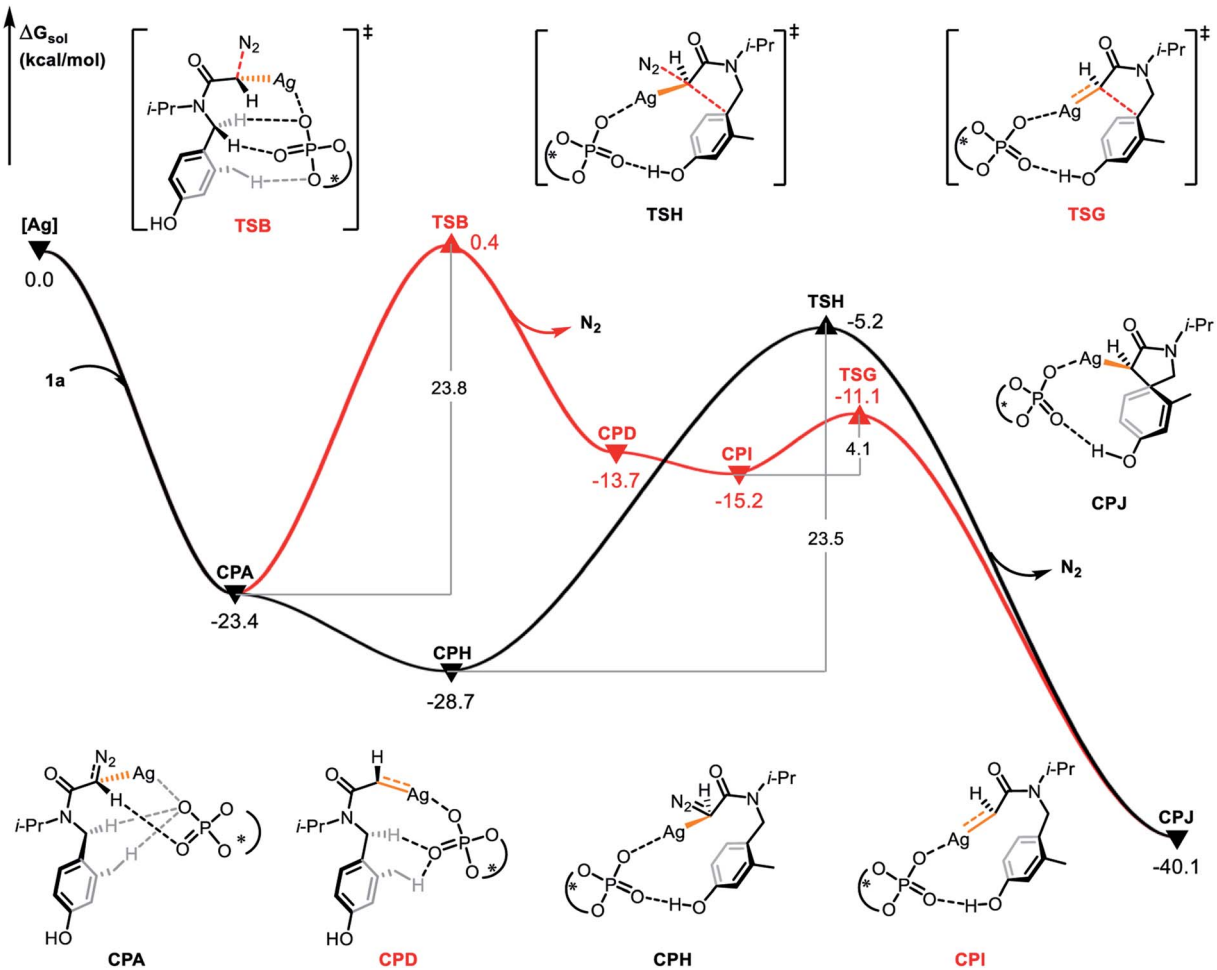

Fig. 6 Gibbs free energy profile (in kcal mol^{-1}) for the electrophilic addition of *S* configuration catalyzed by chiral silver phosphate.

note, **3a** is the bicyclic [5.3.0] derivative and the main product of the Büchner reaction. It is formed through transition state **TS6** with an energy barrier of 7.8 kcal mol^{-1}. Obviously, the energy barrier of each transition state in the Büchner reaction path is lower than in the C–H bond insertion process and on the potential energy surface, the relative free energy of each intermediate and transition state is lower. Therefore, the Büchner reaction process is the most favorable pathway in the intramolecular carbene transfer reaction of α-diazoamide **1a** catalyzed by $Rh_2(OAc)_4$. This is consistent with the experimental result that cycloheptatriene derivative **3a** was obtained with a yield of 26%.

In addition, we also explored the process of carboxylic acid-assisted proto-demetallation to form azaspiro[4.5]decane derivative **2a**, which is shown by the red line in Fig. 4. Firstly, the proton transfer of the phenolic hydroxyl group occurs *via* transition state **TS7** with an energy barrier of 12.0 kcal mol^{-1} to give complex **CP8** and is endergonic by 5.0 kcal mol^{-1}. Subsequently, proto-demetallation occurs *via* transition state **TS8**, which transfers the proton from the oxygen atom of the ligand to the α-carbon atom of the α-diazoamide unit. The energy barrier of this step is as high as 24.2 kcal mol^{-1}. Therefore, the dearomatization process catalyzed by $Rh_2(OAc)_4$ is kinetically unfavorable.

Mechanism of asymmetric dearomatization catalyzed by chiral silver phosphate

In order to explore the origin of the enantioselectivity, we conducted DFT calculations at the level of ωB97XD/6-311+G(d,p)-SDD(Ag). Based on the mechanism of silver-catalyzed chemo- and enantioselective intramolecular dearomatization of indoles calculated by Nemoto's group,[9] we first explored the reaction modes featuring silver-carbene generation and concerted silver-carbene reactivity with diazotization taking place simultaneously with dearomatization. The active catalytic species (*S*)-TRIPAg was chosen as the starting point for the free energy profiles (Fig. 5). Coordination of diazoamide **1a** generates complex **CPA** and denitrogenation occurs *via* transition state **TSB** by cleavage of the C–N bond with an energy barrier of 23.8 kcal mol^{-1} to give silver-carbene complex **CPD**. Subsequently, the silver-carbene **CPD** forms the cyclophane-like intermediate **CPE** after the rotation of the C–N bond. In the cyclophane-like intermediate **CPE**, the distance between the hydrogen atom of the hydroxyl group and the oxygen atom of

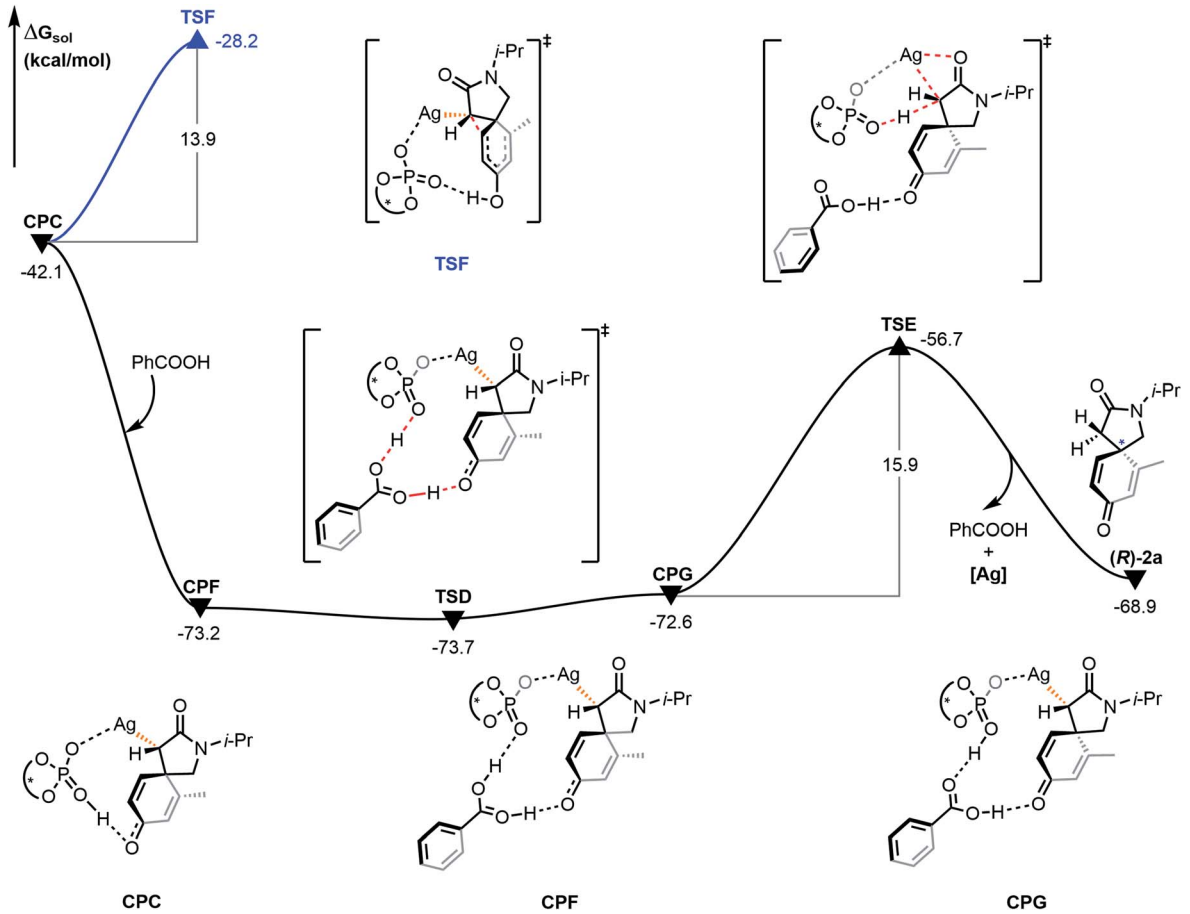

Fig. 7 Gibbs free energy profile (in kcal mol^{-1}) for the proto-demetalation process and Büchner reaction mechanism of *R* configuration catalyzed by chiral silver phosphate.

the phosphate is 1.62 Å, indicating the potential of subsequent electrophilic addition. The hydrogen bond interaction aids in achieving the remote stereocontrol. In the next step, the carbene carbon attacks the carbon at the *ipso* position *via* transition state **TSC** with a barrier of 2.1 kcal mol^{-1}. This produces the spirocyclic intermediate **CPC** and its relative free energy is −42.1 kcal mol^{-1}.

The concerted carbene reaction mode is shown by the black line in Fig. 5. The spirocyclic intermediate **CPC** is directly formed through the transition state **TSA**, and the asynchronous C–C bond formation and C–N bond cleavage process occurs with an energy barrier of 18.7 kcal mol^{-1}, which is the rate-determining step. When comparing the two reaction paths, it is found that the energy barrier of the concerted silver-carbene pathway is 5.1 kcal mol^{-1} lower than that of the stepwise silver-carbene generation mode (**TSA** *vs.* **TSB**). Therefore, the concerted silver-carbene pathway is kinetically more favorable. At the same time, it shows that the concentration of silver-carbene in the reaction is low. The preference for the concerted silver-carbene pathway might be ascribed to the enhanced nucleophilicity of the aryl unit of the α-diazoamide, which has been intramolecularly activated by the phosphate anion, promoting smooth dearomatization before generation of the silver-carbene. For comparision, we have also calculated the pathway to form the (*S*)-spirocyclic intermediate **CPJ** through the concerted addition transition state **TSH** (Fig. 6), the results show that the electrophilic addition of *S* configuration is both kinetically and thermodynamically unfavorable than that of *R* configuration.

The proto-demetalation process assisted by benzoic acid was also calculated (Fig. 7). Association of benzoic acid generates complex **CPF** and is exothermic by 31.1 kcal mol^{-1}. The presence of benzoic acid directly promotes the transfer of the hydroxyl proton. Notably, the free energy of complex **CPG** is 0.6 kcal mol^{-1} higher than that of complex **CPF**, which indicates that the proton migration process is an endergonic and reversible process. Due to the similar energy and no energy barrier between the two complexes, it is feasible for them to be in a rapid equilibrium. In the next step, the complex **CPG** undergoes proto-demetalation through the transition state **TSE** ($\Delta\Delta G^{\neq}$ = 15.9 kcal mol^{-1}). The hydroxyl proton is transferred from the oxygen atom of the phosphate anion to the α-carbon atom of the α-diazoamide unit. At the same time, the silver atom dissociates from the α-carbon atom and coordinates with the carbonyl oxygen atom. Finally, the (*R*)-**2a** product is formed and the catalytic species (*S*)-TRIPAg is regenerated. For

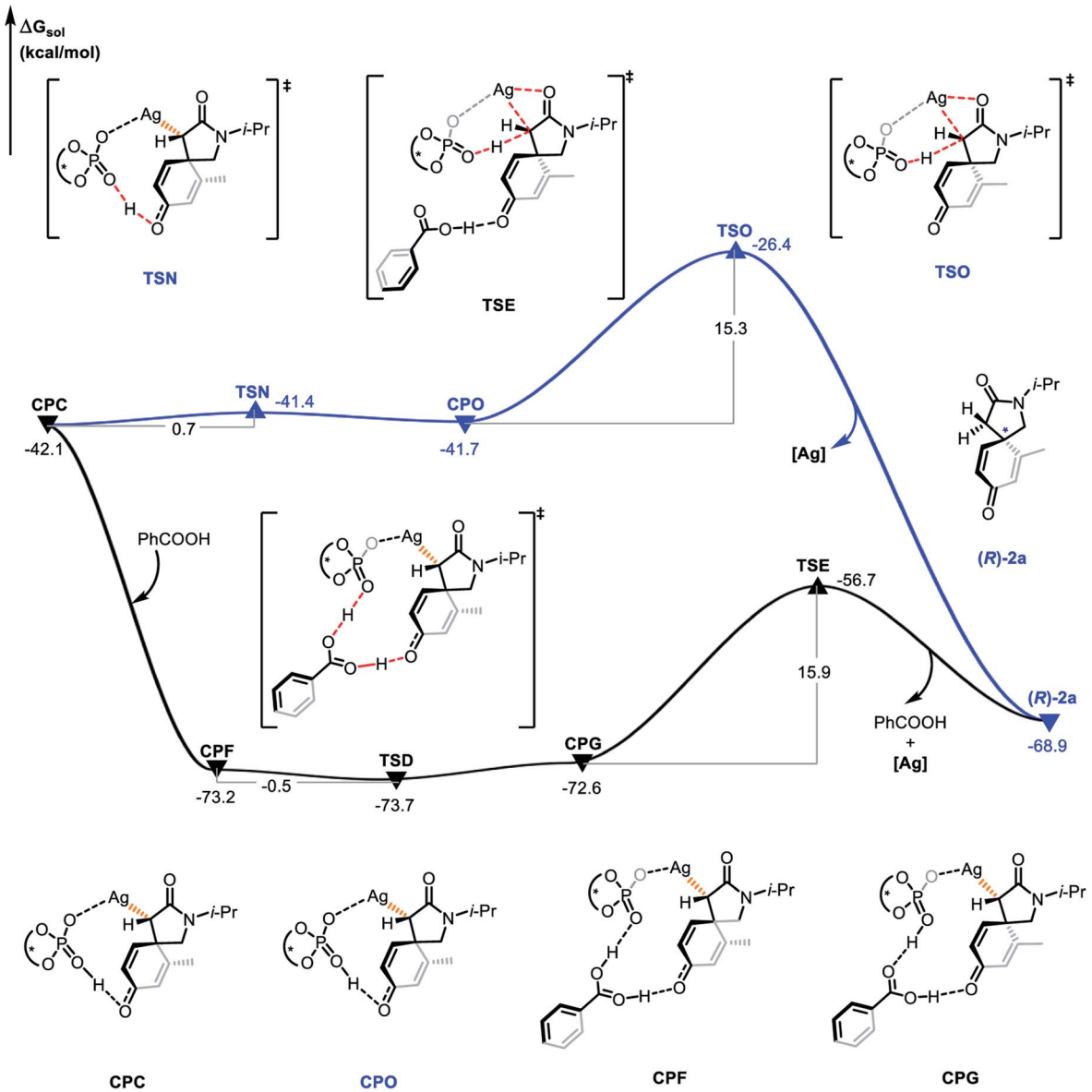

Fig. 8 Gibbs free energy profile (in kcal mol^{-1}) for the proto-demetalation process with or without the assistance of benzoic acid.

a comprehensive theoretical study, we have also calculated this process without the assistance of benzoic acid (Fig. 8). It can be seen that although the activation barriers are very similar (0.7 kcal mol^{-1}, 15.3 kcal mol^{-1} *vs.* −0.5 kcal mol^{-1}, 15.9 kcal mol^{-1}; it is the process with the assistance of acid that is a bit more favorable). The relative free energy for each intermediate and transition state in the presence of benzoic acid is lower than that of the process without the assistance of benzoic acid on the potential energy surface. The role of benzoic acid here is to assist the proto-demetallation process to increase the yield of the desired product without decreasing the enantioselectivity. In 2018, Nemoto's group investigated the role of benzoic acid and pointed out that benzoic acid would promote dissociation of the catalytically inactive homochiral dimer to liberate it for the generation of a monomeric species.[25]

The possible Büchner reaction mechanism was also calculated. The energy barrier of the ring expansion of **CPC** *via* transition state **TSF** is 13.9 kcal mol^{-1}, and the free energy of **TSF** is 45.5 kcal mol^{-1} higher than that of hydrogen transfer transition state **TSD**. Therefore, generation of benzoic acid-associated compounds is kinetically and thermodynamically favorable because of the low relative free energy and no energy barrier, which is consistent with the experimental result that the **3a** product is not formed. Besides, we also compared the process without benzoic acid with Büchner reaction (ESI, Fig. S6†). The results show that the proto-demetalation is favorable as well, which is also nicely consistent with the experimental outcome that only a small amount of **3a** product is found.

In addition to the DFT calculations of above reactions, we have also performed theoretical study for the 1°/3° C–H insertion reaction catalyzed by chiral silver phosphate (ESI, Fig. S1†), the rate-determining step for this process is the carbene formation with an energy barrier of 23.8 kcal mol^{-1}, which is

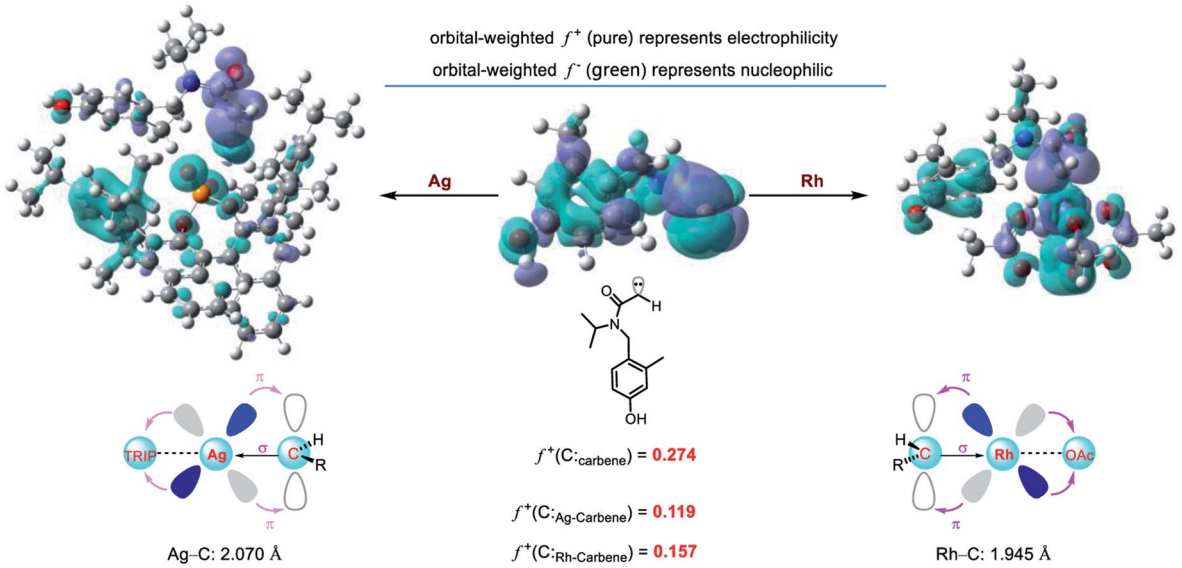

Fig. 9 The orbital weight Fukui function diagram of Ag-carbene and Rh-carbene.

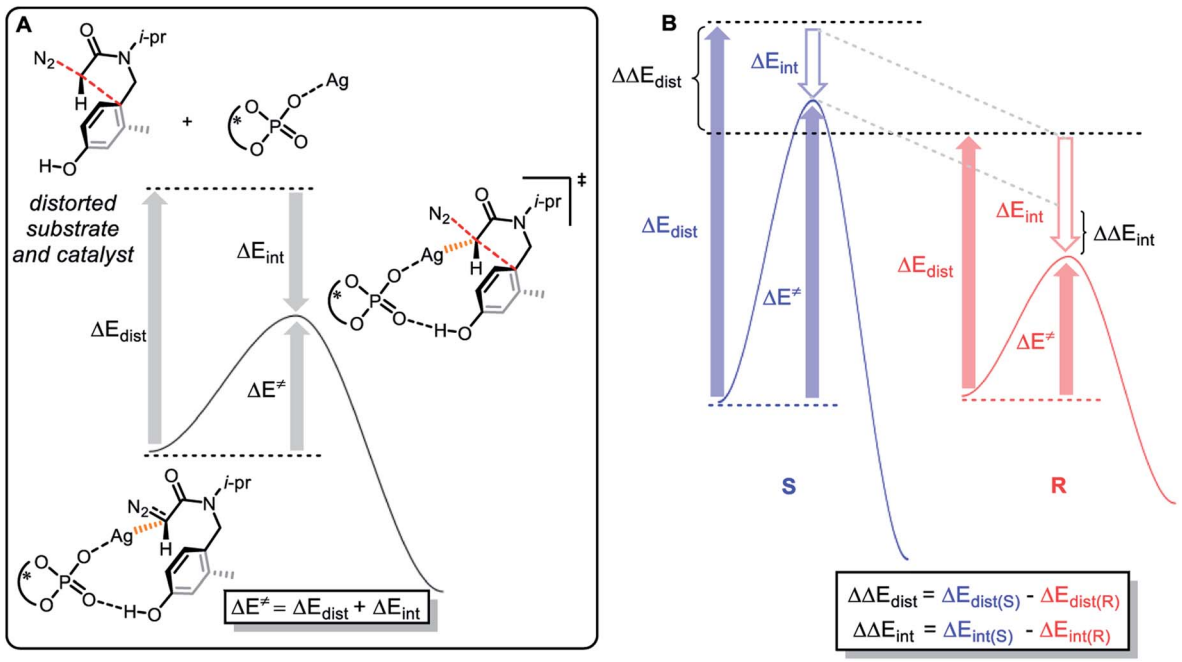

Fig. 10 (A) Definitions of torsional energy and interaction energy; (B) the determining factors of enantioselectivity.

both kinetically and thermodynamically unfavorable compared with the proto-demetalation process, this is also nicely consistent with the experimental results that no C–H insertion products was observed.

Comparison of reactivity between rhodium carbene and silver carbene

To explore the origin of metal-dependent chemo-selectivity, we performed the orbital weight Fukui function to analyze the different catalytic activities between Rh-carbene and Ag-carbene (Fig. 9). The greater the LUMO orbital weight Fukui function (f^+), the stronger its electrophilicity. Thus, the rhodium carbene is more electrophilic than chiral silver phosphate carbene. The chiral phosphate ligand has weak σ-bonding with silver, and the weak π-backdonation effect of the silver $4d^{10}$ orbital, resulting in the weak electrophilicity of the chiral silver phosphate carbene. While the 4d orbitals of the rhodium atom are not completely filled with electrons, and the π-backdonation to the acetic acid ligand is strong, then rhodium accepts more electrons from the carbene carbon, resulting in higher

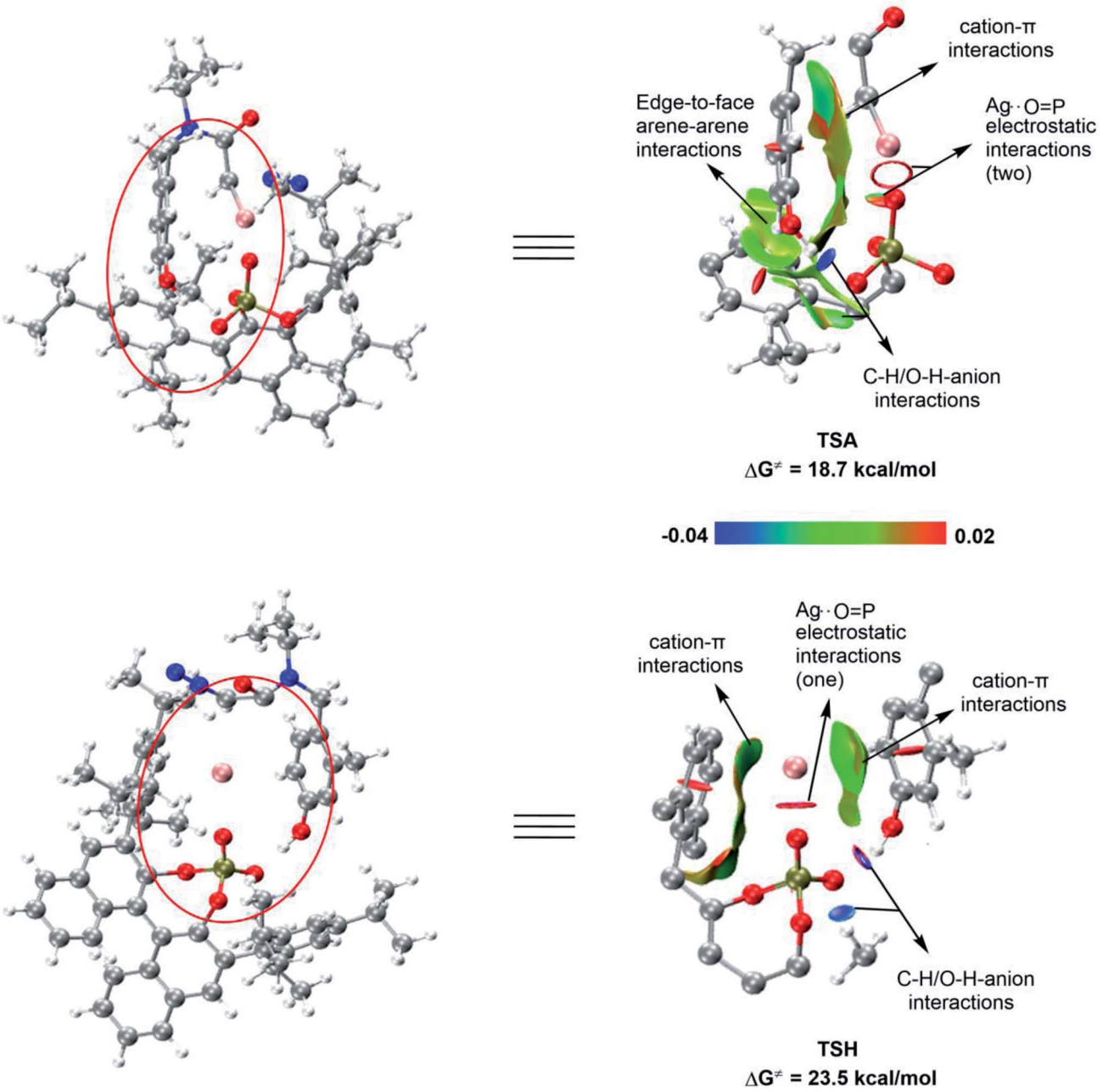

Fig. 11 Non-covalent interaction (NCI) of **TSA** and **TSH** (in order to enhance the readability, we only keep isosurfaces for the key parts involved the interactions of interest and for the convenience to observe the specific positions of these parts, we also put the whole structures of **TSA** and **TSH**). Blue represents strong attraction; green represents van der Waals interaction; red represents strong repulsion or steric effect.

electrophilicity. In addition, we also performed charge decomposition analysis (CDA) and orbital interaction diagram (ESI, Fig. S9†) to study their electrophilicity. It is found that the LUMO energy of Rh-carbene is 0.53 eV lower than that of Ag-carbene, which is easier to accept electrons and shows strong electrophilicity and is consistent with the calculation results of the orbital Fukui function. Therefore, the carboxylic acid anion renders the rhodium carbene more electrophilic and promotes the subsequent intramolecular C–H insertion and Büchner reaction, and the theoretical results are consistent with the experimental phenomena.

However, it is worth noting that ligands can modify the electrophilicity of a metal carbene. Recently, silver-catalyzed site-selective C(sp^3)–H alkylation of alkanes has been developed by our group using donor carbenes.[26] The donor rhodium carbene could not achieve the same results as the silver congener. To explore the difference of electrophilicity between the two-donor metal carbenes, orbital weight Fukui function was also performed. The results show that the donor silver carbene is more electrophilic than the donor rhodium carbene. (f^+(Ag-carbene) = 0.260 *vs.* f^+(Rh-carbene) = 0.135, Fig. S10†).

Table 1 Analysis of torsional energy and interaction energy of electrophilic addition transition state structure

	ΔE_{dist}							
TS	Cat.	Subst.	Total	$\Delta\Delta E_{dist}$	ΔE_{int}	$\Delta\Delta E_{int}$	$\Delta E^{\neq}$	$\Delta\Delta E^{\neq}$
R	4.8	42.7	47.5	6.8	−59.8	4.2	−12.3	11.0
S	9.8	44.5	54.3		−55.6		−1.3	

The origin of the enantioselectivity for silver catalyzed dearomatization

To explore the origin of enantioselectivity, we conducted a distortion–interaction analysis[27] on the concerted addition transition state **TSA** and **TSH** to gather further evidence for the role of ligand steric effect on selectivity. As shown in Fig. 10, this type of analysis involves the decomposition of activation energy ($\Delta E^{\neq}$) into a distortion (ΔE_{dist}) and an interaction term (ΔE_{int}). The distortion term is usually positive (unfavorable), which represents the energy penalty for distorting the reactants into the transition state geometry. The interaction term is usually negative, which represents the favorable interaction between the substrate and the catalyst. The relationship between distortion and interaction is defined as $\Delta E^{\neq} = \Delta E_{dist} + \Delta E_{int}$.

The enantioselectivity is determined by the difference between the distortion and interaction energy of the intramolecular electrophilic addition reaction between the two configurations of *R* and *S* (Fig. 10), which is defined as: $\Delta\Delta E_{dist} = \Delta E_{dist}(S) - \Delta E_{dist}(R)$; $\Delta\Delta E_{int} = \Delta E_{int}(S) - \Delta E_{int}(R)$. According to the results in Table 1, the larger the value of $\Delta\Delta E_{dist}$, the stronger the effect of distortion energy, which means that the *S* configuration reaction is more unfavorable. In addition, interaction energy of *R* configuration is more negative, which shows that the *R* configuration reaction is more favorable. This can be rationalized by (1) the stronger coulombic attraction between Ag and the carbene carbon in the *R* configuration transition state **TSA**, which can be proven by a relatively short distance (**TSH**(*S*), *d*(Ag···C) = 2.10 Å *vs.* **TSA**(*R*), *d*(Ag···C) = 2.05 Å); (2) the ability for another oxygen atom of P═O to interact with Ag; (3) there is also a favorable edge-to-face arene–arene interaction between the arene of the substrate and the ligand (Fig. 11).

To further explore the difference between the key transition states (**TSA** and **TSH**) of the two configurations, we conducted a non-covalent interaction (NCI) analysis (Fig. 11). The results showed that the cation−π interaction between the silver atom and the arene of the substrate, the edge-to-face arene–arene interaction between the aromatic rings of the substrate and the ligand, the C–H/O–H anion interaction, and the Coulombic attraction between silver and the two oxygen atoms of the phosphate effectively stabilizes **TSA**, thereby promoting the smooth progress of the *R* configuration concerted-addition. However, in the transition state **TSH**, no edge-to-face arene–arene interaction between the aromatic rings of the substrate and the ligand was found, and the Coulombic attraction only exists between silver and one oxygen atom of the phosphate. In addition, due to the existence of cation−π interactions between the aromatic rings of substrate and ligand with Ag in **TSH**, the geometry of AgL is more constrained. Therefore, the calculation results show that the reaction of the *S* configuration is relatively less favorable.

Conclusion

Due to the unique coordination mode and catalytic activity of silver, the asymmetric carbene transfer reactions catalyzed by silver have developed slowly for a long time. Based on the first silver-catalyzed high enantioselective carbene transfer reaction published by Nemoto in 2017, we examined the mechanism of silver *versus* rhodium catalysis and revealed the origin of the chemo- and enantioselectivity of the reaction. The calculation results reveal that when silver is used as a catalyst, due to the intramolecular activation of the phosphate anion, the enhanced nucleophilicity of α-diazoacetamide unit results in dearomatization before generation of the silver carbene. When rhodium is used as a catalyst, since the rhodium carbene has stronger electrophilicity, typical carbene reactions are prone to occur. In addition, through energy decomposition analysis based on molecular force field of the key concerted-addition transition state, it is found that the preference for the (*R*)-**2a** product is due to a much smaller distortion disadvantage and a larger interaction energy advantage. Therefore, the dearomatization reaction of the *R* configuration is strongly favored.

Conflicts of interest

There are no conflicts to declare.

Acknowledgements

Financial support was provided by the Fundamental Research Funds for the Central Universities (2412020FZ006), and the Education Department of Jilin Prov. China (JJKH20211283KJ). For work performed in Ghent, the iBOF (C3) and the FWO (fellowship to NVT) are gratefully acknowledged for support.

References

1 (*a*) A. DeAngelis, R. Panish and J. M. Fox, Rh-catalyzed intermolecular reactions of α-alkyl-α-diazo carbonyl compounds with selectivity over β-hydride migration, *Acc. Chem. Res.*, 2016, **49**, 115–127; (*b*) Y. Deng, C. Jing, H. Arman and M. P. Doyle, Reactivity and selectivity in catalytic reactions of enoldiazoacetamides. Assessment of metal carbenes as intermediates, *Organometallics*, 2016, **35**, 3413–3420; (*c*) S. Harada, M. Kono, T. Nozaki, Y. Menjo, T. Nemoto and Y. Hamada, General approach to nitrogen-bridged bicyclic frameworks by Rh-catalyzed formal carbene insertion into an amide C–N bond, *J. Org. Chem.*, 2015, **80**, 10317–10333.

2 (*a*) M. P. Munoz, Silver-catalysed reactions of alkynes: recent advances, *Chem. Soc. Rev.*, 2014, **43**, 3164–3183; (*b*) N. T. Patil and Y. Yamamoto, Coinage metal-assisted synthesis of heterocycles, *Chem. Rev.*, 2008, **108**, 3395–3442.

3 Y. Cui and C. He, Efficient aziridination of olefins catalyzed by a unique disilver(I) compound, *J. Am. Chem. Soc.*, 2003, **125**, 16202–16203.

4 J. M. Alderson, J. R. Corbin and J. M. Schomaker, Tunable, chemo- and site-selective nitrene transfer reactions through the rational design of silver(I) catalysts, *Acc. Chem. Res.*, 2017, **50**, 2147–2158.

5 G. L. Hamilton, E. J. Kang, M. Mba and F. D. Toste, A powerful chiral counterion strategy for asymmetric transition metal catalysis, *Science*, 2007, **317**, 496–499.

6 (*a*) R. R. Nani and S. E. Reisman, α-Diazo-β-ketonitriles: uniquely reactive substrates for arene and alkene cyclopropanation, *J. Am. Chem. Soc.*, 2013, **135**, 7304–7311; (*b*) V. N. G. Lindsay, D. Fiset, P. J. Gritsch, S. Azzi and A. B. Charette, Stereoselective Rh_2(S-IBAZ)$_4$-Catalyzed Cyclopropanation of Alkenes, Alkynes, and Allenes: Asymmetric Synthesis of Diacceptor Cyclopropylphosphonates and Alkylidenecyclopropanes, *J. Am. Chem. Soc.*, 2013, **135**, 1463–1470; (*c*) V. K.-Y. Lo, Z. Guo, M. K.-W. Choi, W.-Y. Yu, J.-S. Huang and C.-M. Che, Highly Selective Intramolecular Carbene Insertion into Primary C–H Bond of α-Diazoacetamides Mediated by a (*p*-Cymene)ruthenium(II) Carboxylate Complex, *J. Am. Chem. Soc.*, 2012, **134**, 7588–7591; (*d*) Z. Yu, B. Ma, M. Chen, H.-H. Wu, L. Liu and J. Zhang, Highly Site-Selective Direct C–H Bond Functionalization of Phenols with α-Aryl-α-diazoacetates and Diazooxindoles *via* Gold Catalysis, *J. Am. Chem. Soc.*, 2014, **136**, 6904–6907.

7 (*a*) Y. Xi, Y. Su, Z. Yu, B. Dong, E. J. McClain, Y. Lan and X. Shi, Chemoselective carbophilic addition of α-diazoesters through ligand-controlled gold catalysis, *Angew. Chem., Int. Ed.*, 2014, **53**, 9817–9821; (*b*) Y. Liu, Z. Yu, J. Z. Zhang, L. Liu, F. Xia and J. Zhang, Origins of unique gold-catalysed chemo- and site-selective C-H functionalization of phenols with diazo compounds, *Chem. Sci.*, 2016, **7**, 1988–1995.

8 (*a*) M. Alvarez-Corral, M. Munoz-Dorado and I. Rodriguez-Garcia, Enantioselective silver-catalyzed transformations, *Chem. Rev.*, 2008, **108**, 3174–3198; (*b*) Q. Z. Zheng and N. Jiao, Ag-catalyzed C–H/C–C bond functionalization, *Chem. Soc. Rev.*, 2016, **45**, 4590–4627; (*c*) J. M. Weibel, A. Blanc and P. Pale, Ag-mediated reactions: coupling and heterocyclization reactions, *Chem. Rev.*, 2008, **108**, 3149–3173; (*d*) K. Sekine and T. Yamada, Silver-catalyzed carboxylation, *Chem. Soc. Rev.*, 2016, **45**, 4524–4532; (*e*) R. Karmakar and D. Lee, Reactions of arynes promoted by silver ions, *Chem. Soc. Rev.*, 2016, **45**, 4459–4470; (*f*) U. Halbes-Letinois, J. M. Weibel and P. Pale, The organic chemistry of silver acetylides, *Chem. Soc. Rev.*, 2007, **36**, 759–769; (*g*) G. Fang and X. Bi, Silver-catalysed reactions of alkynes: recent advances, *Chem. Soc. Rev.*, 2015, **44**, 8124–8173.

9 H. Nakayama, S. Harada, M. Kono and T. Nemoto, Chemoselective Asymmetric Intramolecular Dearomatization of Phenols with α-Diazoacetamides Catalyzed by Silver Phosphate, *J. Am. Chem. Soc.*, 2017, **139**, 10188–10191.

10 S. Harada, K. Tanikawa, H. Homma, C. Sakai, T. Ito and T. Nemoto, Silver-catalyzed asymmetric insertion into phenolic O-H bonds using aryl diazoacetates and theoretical mechanistic studies, *Chem.–Eur. J.*, 2019, **25**, 12058–12062.

11 T. Shi, S. Teng, A. G. K. Reddy, X. Guo, Y. Zhang, K. H. Moore, T. Buckley, D. J. Mason, W. Wang, E. Chapman and W. Hu, Catalytic asymmetric synthesis of 2,5-dihydrofurans using synergistic bifunctional Ag catalysis, *Org. Biomol. Chem.*, 2019, **17**, 8737–8744.

12 G. L. Hamilton, E. J. Kang, M. Mba and F. D. Toste, A powerful chiral counterion strategy for asymmetric transition metal catalysis, *Science*, 2007, **317**, 496–499.

13 S. Bachmann, D. Fielenbach and K. A. Jørgensen, Cu(I)-carbenoid- and Ag(I)-Lewis acid-catalyzed asymmetric intermolecular insertion of α-diazo compounds into N–H bonds, *Org. Biomol. Chem.*, 2004, **2**, 3044–3049.

14 K. Burgess, H.-J. Lim, A. M. Porte and G. A. Sulikowski, New catalysts and conditions for a C–H insertion reaction identified by high throughput catalyst screening, *Angew. Chem., Int. Ed.*, 1996, **35**, 220–222.

15 J. Ueda, S. Harada, A. Kanda, H. Nakayama and T. Nemoto, Silver-catalyzed, chemo- and enantioselective intramolecular dearomatization of indoles to access sterically congested azaspiro grameworks, *J. Org. Chem.*, 2020, **85**, 10934–10950.

16 T. Ito, S. Harada, H. Homma, *et al.*, Asymmetric intramolecular dearomatization of nonactivated arenes with ynamides for rapid assembly of fused ring system under silver catalysis, *J. Am. Chem. Soc.*, 2021, **143**, 604–611.

17 M. J. Frisch, G. W. Trucks, H. B. Schlegel, G. E. Scuseria, M. A. Robb, J. R. Cheeseman, G. Scalmani, V. Barone, G. A. Petersson, H. Nakatsuji, X. Li, M. Caricato, A. V. Marenich, J. Bloino, B. G. Janesko, R. Gomperts, B. Mennucci, H. P. Hratchian, J. V. Ortiz, A. F. Izmaylov, J. L. Sonnenberg, D. Williams-Young, F. Ding, F. Lipparini, F. Egidi, J. Goings, B. Peng, A. Petrone, T. Henderson, D. Ranasinghe, V. G. Zakrzewski, J. Gao, N. Rega, G. Zheng, W. Liang, M. Hada, M. Ehara, K. Toyota, R. Fukuda, J. Hasegawa, M. Ishida, T. Nakajima, Y. Honda, O. Kitao, H. Nakai, T. Vreven, K. Throssell, J. A. Montgomery Jr, J. E. Peralta, F. Ogliaro, M. J. Bearpark, J. J. Heyd, E. N. Brothers, K. N. Kudin, V. N. Staroverov, T. A. Keith, R. Kobayashi, J. Normand, K. Raghavachari, A. P. Rendell, J. C. Burant, S. S. Iyengar, J. Tomasi, M. Cossi, J. M. Millam, M. Klene, C. Adamo, R. Cammi, J. W. Ochterski, R. L. Martin, K. Morokuma, O. Farkas, J. B. Foresman and D. J. Fox, *Gaussian 16, Revision C.01*, Gaussian, Inc., Wallingford CT, 2019.

18 (*a*) A. D. A. Becke, New Mixing of Hartree-Fock and Local Density-functional Theories, *J. Chem. Phys.*, 1993, **98**, 1372–1377; (*b*) A. D. Becke, Density-functional Thermochemistry. III. The Role of Exact Exchange, *J. Chem. Phys.*, 1993, **98**, 5648–5652.

19 S. Grimme, S. Ehrlich and L. Goerigk, Effect of the damping function in dispersion corrected density functional theory, *J. Comput. Chem.*, 2011, **32**, 1456–1465.

20 (*a*) L. von Szentpály, P. Fuentealba, H. Preuss and H. Stoll, Pseudopotential calculations on Rb^{+2}, Cs^{+2}, RbH^{+}, CsH^{+} and the mixed alkali dimer ions, *Chem. Phys. Lett.*, 1982, **93**, 555–559; (*b*) P. Schwerdtfeger, M. Dolg, W. H. E. Schwarz, G. A. Bowmaker and P. D. W. Boyd, Relativistic effects in gold chemistry. I. Diatomic gold compounds, *J. Chem. Phys.*, 1989, **91**, 1762–1774; (*c*) M. Dolg, U. Wedig, H. Stoll and H. Preuss, Energy-adjusted *ab initio* pseudopotentials for the first row transition elements, *J. Chem. Phys.*, 1987, **86**, 866–872.

21 (*a*) K. Fukui, Formulation of the reaction coordinate, *J. Phys. Chem.*, 1970, **74**, 4161–4163; (*b*) K. Fukui, The path of chemical reactions - the IRC approach, *Acc. Chem. Res.*, 1981, **14**, 363–368.

22 A. V. Marenich, C. J. Cramer and D. G. Truhlar, Universal solvation model based on solute electron density and on a continuum model of the solvent defined by the bulk dielectric constant and atomic surface tensions, *J. Phys. Chem. B*, 2009, **113**, 6378–6396.

23 (*a*) T. Lu and F. Chen, Multiwfn: A multifunctional wavefunction analyzer, *J. Comput. Chem.*, 2012, **33**, 580–592, accessed August, 2020, available at: **https://www.sobereva.com/multiwfn**; (*b*) E. R. Johnson, S. Keinan, P. Mori-Sánchez, J. Contreras-García, A. J. Cohen and W. Yang, Revealing Noncovalent Interactions, *J. Am. Chem. Soc.*, 2010, **132**, 6498–6506; (*c*) T. Lu, Z. Liu and Q. Chen, Comment on "18 and 12 - Member carbon rings (cyclo[*n*] carbons) - A density functional study", *Mater. Sci. Eng., B*, 2021, **273**, 115425–115428.

24 C. Y. Legault, *CYLview, version 1.0b*, Université de Sherbrooke, Canada, 2009.

25 H. Nakayama, S. Harada, A. Kanda, I. M.-Y. Kwork and T. Nemoto, Binary additive effect of benzoic acid in ipso-Friedel-Crafts-type dearomatization of phenols using a chiral silver phosphate, *Tetrahedron*, 2018, **74**, 2435–2439.

26 Z. Liu, S. Cao, W. Yu, J. Wu, F. Yi, E. A. Anderson and X. Bi, Site-Selective C–H Benzylation of Alkanes with *N*-Triftosylhydrazones Leading to Alkyl Aromatics, *Chem*, 2020, **6**, 2110–2124.

27 F. M. Bickelhaupt and K. N. Houk, Analyzing reaction rates with the distortion/interaction-activation strain model, *Angew. Chem., Int. Ed.*, 2017, **56**, 10070–10086.